


Single Beam Acoustical Tweezers Based on Focused Beams: A Numerical Analysis of Two-Dimensional and Three-Dimensional Trapping Capabilities

Zhixiong Gong¹ and Michael Baudoin^{1,2,*†}

¹Univ. Lille, CNRS, Centrale Lille, Univ. Polytechnique Hauts-de-France, UMR 8520 - IEMN - Institut d'Électronique de Microélectronique et de Nanotechnologie, Lille F-59000, France

²Institut Universitaire de France, 1 rue Descartes, 75005, Paris

 (Received 20 May 2022; revised 31 August 2022; accepted 15 September 2022; published 13 October 2022)

Selective single beam tweezers open tremendous perspectives in microfluidics and microbiology for the micromanipulation, assembly, and mechanical properties testing of microparticles, cells, and microorganisms. In optics, single beam optical tweezers rely on tightly focused laser beams, generating a three-dimensional (3D) trap at the focal point. In acoustics, 3D traps have so far only been reported experimentally with specific wavefields called acoustical vortices. Indeed, many types of particles are expelled (not attracted to) the center of a focused beam. Yet the trapping capabilities of focused beams have so far only been partially explored. In this paper, we numerically explore with an angular spectrum code the trapping capabilities of focused beams on a wide range of parameters (size over wavelength ratio and type of particles). We demonstrate that (i) 3D trapping of particles, droplets, and microorganisms more compressible than the surrounding fluid is possible *in and beyond the Rayleigh regime* [e.g., polydimethylsiloxane (PDMS), olive oil, benzene, and lipid sphere] and that (ii) 2D trapping (without an axial trap) of particles with positive contrast factor can be achieved by using the particles resonances. The 3D trapping of biocompatible functionalized PDMS particles with integrable, high-frequency focused-beam tweezers opens the way towards acoustic force spectroscopy in some force ranges that were not accessible with optical methods.

DOI: [10.1103/PhysRevApplied.18.044033](https://doi.org/10.1103/PhysRevApplied.18.044033)

I. INTRODUCTION

Three-dimensional (3D) microparticle trapping with single beam optical tweezers was demonstrated by Ashkin *et al.* in 1986 with a focused laser beam under the condition that the particle's refractive index is higher than that of the surrounding fluid medium [1]. The advantages of using a simple focused beam to manipulate particles include the following. (i) Simplicity: a focused beam is easy to produce with a simple lens. (ii) Excellent selectivity: the beam is focused on the target particle and hence has little effect on the neighboring ones. (iii) Strong trap: a focused beam leads to strong gradients near the focal point that are thus suitable for creating strong traps.

In acoustics, the first to consider focused beams to trap objects was Wu in 1991 [2]. But Wu used two collimated beams (not a single beam) propagating in opposite directions to obtain an acoustic trap for latex particles and clusters of frog eggs. By *single beam* we mean a beam whose energy comes from only one direction of space. Single beam tweezers are more convenient to use

experimentally since they do not require putting sources or reflectors all around the target objects. Later on in 2009, as an analogy to optical tweezers, Shung's group [3] explored the possibilities offered by single focused beams to trap particles. In their pioneering work, they succeeded to trap laterally (hence in two dimensions) oleic acid lipid droplets with a single beam at around 30 MHz in the Mie regime (with $a/\lambda \approx 1.26$, where a designates the particle radius and λ the wavelength). However, axial trapping was not demonstrated. In addition, the ray method used to guide and analyze their experiments [4,5] was used beyond its limit of validity since such a method can only be used when $a \gg \lambda$. Later on, the same group experimentally demonstrated 2D trapping of a single elastic particle and human cell beyond the Rayleigh regime with focused beam tweezers at frequencies up to 400 MHz [6–9]. Note that the Rayleigh regime corresponds to the long-wavelength regime wherein $a \ll \lambda$, while the Mie regime corresponds to $a \gtrsim \lambda$. They also performed calibration and measurement of sound forces on liquid droplets [10,11]. All these demonstrations were however limited to 2D traps. Then, Silva *et al.* [12] numerically explored with partial wave expansion the possibility of trapping droplets in three dimensions with focused beams. They

*Corresponding author. michael.baudoin@univ-lille.fr

†<http://films-lab.univ-lille1.fr/michael>

theoretically showed that a 3D trap can be obtained in the Rayleigh regime for a specific silicone-oil droplet with a density of 1004 kg/m^3 , close to that of water, and compressibility of $1050 \times 10^{-12} \text{ Pa}$, i.e., more than 2 times that of water. However, (i) the trap was obtained only with droplets more compressible than the surrounding phase, and (ii) 3D trapping beyond the Rayleigh regime was not explored. More recently, Yang *et al.* [13] reported the levitation upward of a relatively large polydimethylsiloxane (PDMS) particle of radius 400 to 800 μm induced by a 1 MHz focused beam in the regime $a/\lambda \in [0.26, 0.52]$. Again, 3D trapping was not demonstrated in this regime. Finally, it is worth noting that 3D trapping of millimetric carbon tetrachloride droplets surrounded by water medium has been demonstrated in the near field of a fraxicon lens [14]. However, in this case, the insufficient axial focalization of the acoustic field does not provide enough energy localization to create a selective trap (acting mainly on the target object).

Experimentally, 3D trapping against the gravity of particles denser and stiffer than the surrounding phase with a single beam has only been demonstrated with specific wavefields called focused acoustical vortices [15], some helical wave spinning around a phase singularity [16]. Indeed, as we will see in this paper, 3D particle trapping of these types of particles is not possible at the center of a focused beam. With acoustical vortices, 2D trapping of small microparticles [17,18] and cells [19] has also been demonstrated with holographic tweezers based on spiraling interdigitated transducers [20]. Later on, it was theoretically shown [21] that these types of particles could also be trapped in three dimensions with these types of devices. The 3D manipulation of bubbles with axial compensation of the Archimedes force and radiation force with these wave structures was also demonstrated by Baresch *et al.* [22].

Yet, (i) as discussed in the first paragraph, tweezers based on focused beams would have many advantages in terms of simplicity, selectivity, and trapping force compared to their vortex counterparts, and (ii) their trapping capabilities have only been partially explored. In this paper, we numerically investigate with an angular spectrum code [19,23,24] the trapping capabilities of a focused beam on a wide range of parameters (size and type of particles or droplets) in and beyond the Rayleigh regime. We demonstrate that (i) 3D trapping is possible for some elastic and fluid particles more compressible than the surrounding phase (e.g., PDMS, olive oil, and benzene) in the Rayleigh regime and also at some specific frequencies beyond the Rayleigh regime, (ii) only 2D lateral trapping of the most common elastic particles used in experiments [Pyrex, polystyrene (PS), and polyethylene (PE)] can be achieved at specific frequencies in the Mie regime, and that (iii) typical human cells cannot be trapped in three dimensions in a spherical focused beam, while lipid (fat)

cell 3D trapping is possible at some specific frequencies. This work is organized as follows. Sec. II describes how focused beams can be synthesized with holographic transducers. Sections III B and III B give overviews of the angular spectrum method and of the generalized Gor'kov theory used in this paper to compute the radiation force for arbitrary particle size and in the Rayleigh regime, respectively. Sections IV A and IV B discuss the 2D and 3D trapping abilities for two groups of particles, while biological particles are addressed in Sec. IV C.

II. SYNTHESIS OF FOCUSED BEAMS WITH ACTIVE HOLOGRAMS

It was recently shown by our team that complex high-frequency acoustic fields such as focused acoustical vortices can be synthesized by using active holograms based on interdigitated transducers [16–18,20]. In short, the binarized phase hologram of the targeted wavefield is materialized by a set of metallic electrodes of inverse polarity deposited at the surface of a piezoelectric substrate. While holograms are generally passive and require an external source, here the signal is directly synthesized by the electrode hologram that activates the piezoelectric substrate. The advantage of this method is that the transducers are flat, transparent, miniaturizable, and can produce high-frequency signals to trap small particles and can be adapted to synthesize arbitrary wavefields.

The simulations of this paper are conducted with realistic fields, produced by binary phase holograms designed to produce focused beams at 40 MHz (which corresponds to a wavelength of $\lambda \approx 37.5 \mu\text{m}$ in water). The design of the electrodes is simply obtained by taking the intersection of a converging focused beam with a source plane [see Fig. 1(a)] and determining two sets of equiphase lines in opposition of phase, which constitutes a binary hologram of the targeted wavefield [see Fig. 1(b)]. An ideal converging spherical focused beam is described in the spherical coordinates (r, θ, φ) as

$$p^*(r, \theta, \varphi, t) = p_0 e^{i(kr - \omega t)} / r, \quad (1)$$

where p_0 is the wave amplitude, $k = \omega/c$ is the wave number, c is the speed of sound, and t is the time. Hence, the equiphase surfaces simply correspond to

$$\phi = \arg(p^*) = kr - \omega t = C + 2n\pi, \quad (2)$$

where C is a constant, n is an arbitrary integer, and the time t can be chosen arbitrarily and is hence chosen as $t = 0$ in the following calculation. To obtain the intersection of these equiphase spherical surfaces with the source plane, we must introduce the cylindrical coordinates (R, φ, z) , taking z as a constant $z = h$ in Eq. (2), where h is the distance between the source plane and the focal point O

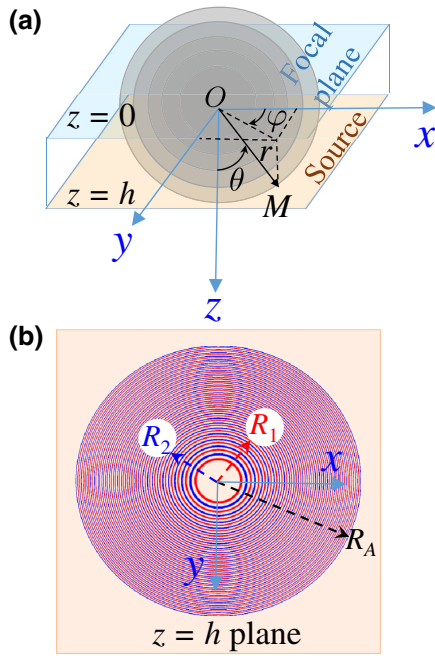


FIG. 1. (a) Sketch representing the source ($z = h$), target ($z = 0$) planes, and spherical coordinates. (b) The structures of the interdigitated transducers are obtained by the intersection of the source plane and the converging spherical waves, as shown in (a). Here R_1 and R_2 are the radii of the two sets of equiphase circles with a phase shift π ; R_A is the aperture radius of the transducer.

[Fig. 1(a)]. Since $R = \sqrt{r^2 - z^2}$, we simply obtain the following equations for the radii of the two sets of electrodes of opposite phases:

$$R_1 = \frac{1}{k} \sqrt{(C + 2n\pi)^2 - (kh)^2}, \quad (3)$$

$$R_2 = \frac{1}{k} \sqrt{[C + (2n + 1)\pi]^2 - (kh)^2}. \quad (4)$$

Note that the arbitrary constant C must be chosen so that $C > kh$ and that each value of n corresponds to a set of two electrodes. Hence, the aperture of the transducer can be fixed by setting the maximum value N of n , with $n \in [0, N]$. Here, N is chosen as 26 to obtain an aperture angle

of approximately 60° for a focal depth of $h = 1$ mm with aperture radius $R_A = 1.72$ mm.

Compared to the binary holograms of focused acoustic vortices, the geometrical radii of the electrodes do not evolve with the azimuthal angle, resulting in two sets of circular concentric circles instead of spiraling ones. The focalization results from the decrease of the radial distance between two consecutive electrodes following the principle of Fresnel lenses. The width of the electrodes is chosen as half the distance between two consecutive electrodes of inverse polarity given by Eqs. (3) and (4). The pressure and velocity fields produced by these transducers are calculated with an angular spectrum method [19,23,24] and represented in Fig. 2. The angular spectrum simply consists in (i) taking the 2D Fourier transform of the source to transform it into a sum of plane waves, (ii) propagating each plane wave up to the target plane, and (iii) taking the inverse Fourier transform of the sum of the transported plane waves [21].

III. CALCULATION OF THE ACOUSTIC RADIATION FORCE

A. General case

The next step is to compute the radiation force that would be exerted on a particle depending on its position, size, and composition. Different analytical formulations of the radiation force exerted by an arbitrary acoustic field on an arbitrary spherical particle have been derived by Silva [25], Baresch *et al.* [26], and Sapozhnikov and Bailey [23], whose equivalence has been demonstrated by Gong and Baudoin [24]. Note that the acoustic radiation torque can also be calculated using the formulas proposed in Refs. [27,28]. Here we use a homemade MATLAB[®] code published in the Supplementary Information of Ref. [19] based on the angular spectrum method [23] to compute the acoustic radiation force, which is more direct considering that we also compute the acoustic field produced by the phase hologram with the angular spectrum method. Hence, the force is calculated using the following formulas from Refs. [21,24]:

$$F_x = \frac{1}{4\pi^2 \rho_0 k^2 c^2} \operatorname{Re} \left\{ \sum_{n=0}^{\infty} \sum_{m=-n}^n C_n (-b_{n+1}^{-m} H_{nm} H_{n+1,m-1}^* + b_{n+1}^m H_{nm} H_{n+1,m+1}^*) \right\}, \quad (5a)$$

$$F_y = \frac{1}{4\pi^2 \rho_0 k^2 c^2} \operatorname{Im} \left\{ \sum_{n=0}^{\infty} \sum_{m=-n}^n C_n b_{n+1}^m (H_{n,-m} H_{n+1,-m-1}^* + H_{nm} H_{n+1,m+1}^*) \right\}, \quad (5b)$$

$$F_z = -\frac{1}{2\pi^2 \rho_0 k^2 c^2} \operatorname{Re} \left\{ \sum_{n=0}^{\infty} \sum_{m=-n}^n C_n c_{n+1}^m H_{nm} H_{n+1,m}^* \right\}. \quad (5c)$$

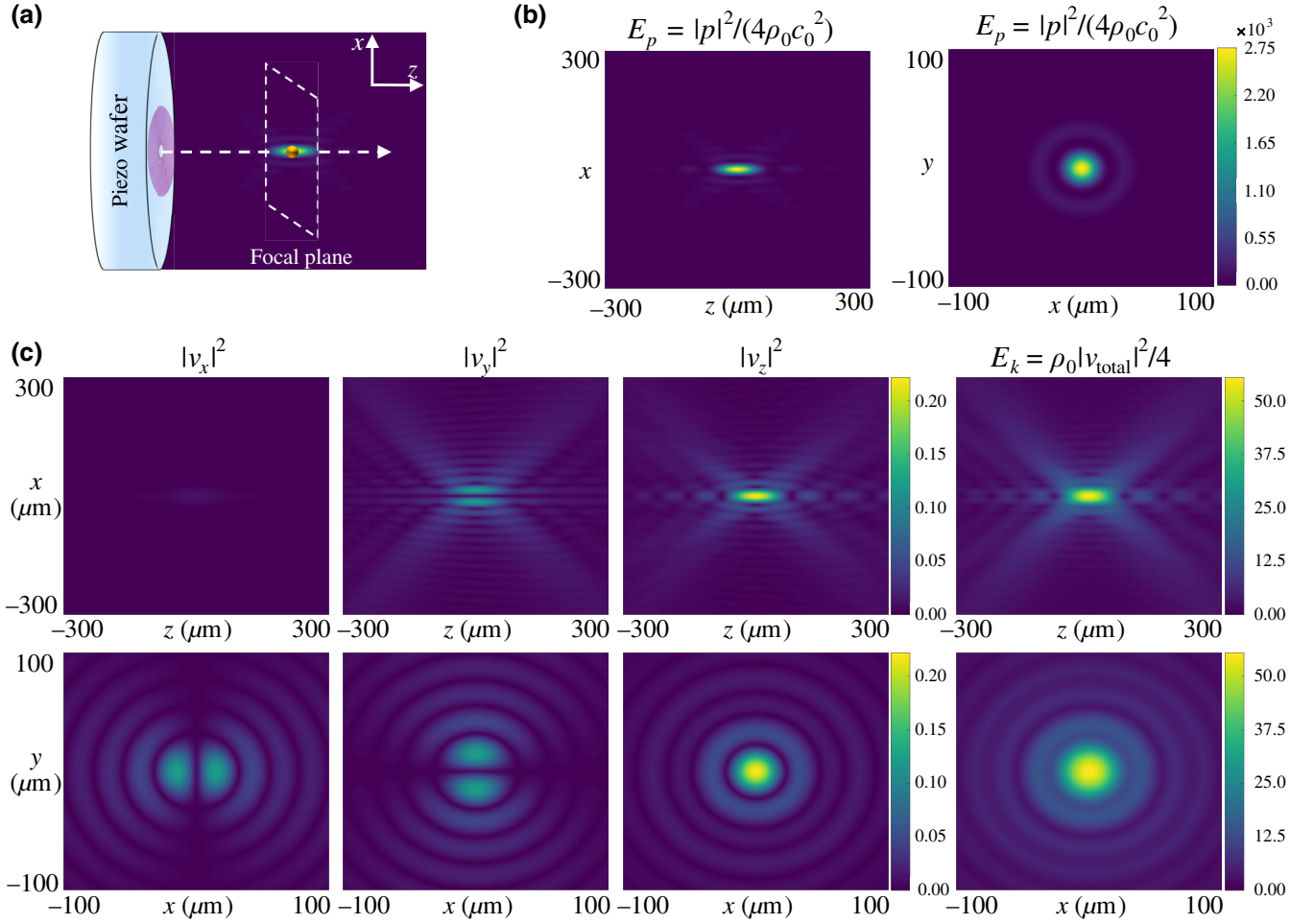


FIG. 2. (a) Schematic of a focused beam of finite aperture 60° synthesized by binary phase holograms representing the signal that would be generated by circular interdigitated transducers. The shapes of the circular electrodes are given in the enlarged figure with the designed principle given in Sec. II. (b) The acoustic potential energy $E_p = |p|^2 / (4\rho_0 c_0^2)$ (in J/m^3 units) in the $(x, y = 0, z)$ and $(x, y, z = 0)$ planes. The pressure amplitude in the source plane is 0.1 MPa for all the simulations. (c) The square amplitudes of the three components of the acoustic velocity $|v_{x,y,z}|^2$ (in m^2/s^2 units) and the kinetic energy $E_k = \rho_0 |\mathbf{v}_{\text{total}}|^2 / 4$ (in J/m^3 units) are depicted in the $(x, y, z = 0)$ plane in the upper row, and in the $(x, y = 0, z)$ plane in the lower row. The information is helpful to understand the trapping properties of Rayleigh particles (size much smaller than the wavelength) in three dimensions.

Here $C_n = A_n + 2A_n A_{n+1}^* + A_{n+1}^*$, the A_n^m are the beam shape coefficients, $b_n^m = \sqrt{[(n+m)(n+m+1)] / [(2n-1)(2n+1)]}$, and $c_n^m = \sqrt{[(n+m)(n-m)] / [(2n-1)(2n+1)]}$. Note that here the partial wave coefficients A_n^m reduce to A_n owing to the spherical shape of the particle. The radiation force for general shapes can be obtained from Eq. (13) of Ref. [24] with C_n^m and $C_n^{m\mp 1}$ given therein. The term H_n^m describes the incident beam shape coefficients and is related to the angular spectrum in a transverse plane with the explicit expression given in Eq. (2) of Ref. [21]. By ρ_0 and c we denote the mass density and sound speed in the medium.

B. Simplification in the Rayleigh regime

When the particles are much smaller than the wavelength, i.e., in the Rayleigh regime, the radiation force formulas for spherical particles in Eqs. (5) simplify to [23]

$$\mathbf{F} = V_0 \left\{ -\nabla \left[f_1 \left(\frac{|p|^2}{4\rho_0 c_0^2} \right) - f_2 \left(\frac{\rho_0 |\mathbf{v}|^2}{4} \right) \right] + \frac{(ka)^3}{3} \left[\left(f_1^2 + \frac{2f_1 f_2}{3} \right) \text{Re} \left(\frac{k}{2c_0} p \mathbf{v}^* \right) - \frac{f_2^2}{3} \text{Im} \left(\frac{\rho_0}{2} \mathbf{v} \cdot \nabla \mathbf{v}^* \right) \right] \right\}, \quad (6)$$

where $V_0 = 4/3 \pi a^3$ is the volume of the spherical shape with particle radius a , and $f_1 = 1 - \kappa_p/\kappa_0$ and $f_2 = 3(\rho_p - \rho_0)/(2\rho_p + \rho_0)$ are the monopolar and dipolar acoustic contrast factors. The κ_p/κ_0 and ρ_p/ρ_0 ratios are the compressibility contrast and density contrast between the particle and the surrounding fluid, respectively. The “ p ” subscript represents the particle and the “ 0 ” subscript describes the surrounding medium. Note that the definition of f_2 here is different from that in Gor’kov’s original work with a ratio of $3/2$ in order to have a compact expression related to the kinetic energy. We denote by p and \mathbf{v} the complex pressure and velocity of the incident acoustic fields, “Re” and “Im” respectively designate the real and imaginary parts of a complex number, and the “ $*$ ” superscript stands for the complex conjugate. The first term in the curly braces of Eq. (6) is nothing but the seminal Gor’kov expression of the radiation force introduced in Ref. [29], which describes the contribution of a gradient force $\mathbf{F}_{\text{grad}} = -\nabla U$, with $U = V_0[f_1(|p|^2/4\rho_0 c_0^2) - f_2(\rho_0|\mathbf{v}|^2/4)]$ the so-called Gor’kov potential. The remaining terms correspond to the scattering force \mathbf{F}_{scat} contributions. Note that, for a standing wave, the second and third terms vanish, while for a plane progressive wave, the Gor’kov gradient force vanishes since $|p|^2$ and $|\mathbf{v}|^2$ are homogeneous. Also, as can be seen from this formula, the gradient force is proportional to $O((ka)^3)$, while the scattering force is proportional to $O((ka)^6)$, so that the gradient forces are generally dominant (if they do not vanish) over the scattering force in the Rayleigh regime. In addition, the absorption-induced radiation force is significantly smaller than the scattering-induced radiation force [30]. Hence, it can be ignored compared to the gradient force. Note that the radiation force formula, Eq. (1), of Ref. [15] [and hence, Eq. (3) of Ref. [31]] has a typographical error: a ratio of 2 is missing before the $f_1 f_2$ term in the second line. We have checked that Eq. (77) of Ref. [23] is correct and reorganized it herein as Eq. (6).

In the expression of the gradient force, the first term is proportional to the monopolar acoustic contrast factor $f_1 = 1 - \kappa_p/\kappa_0$ and the acoustic potential energy density $E_p = |p|^2/4\rho_0 c_0^2$. Hence, this term is related to the relative compression and expansion of the particle compared to the surrounding fluid. Particles less compressible than the surrounding fluid, $f_1 > 0$ (respectively more compressible, $f_1 < 0$), are hence pushed by this term toward the pressure amplitude minima (respectively maxima) of a wavefield in the Rayleigh regime. The second term of the gradient force is proportional to the dipolar acoustic contrast factor $f_2 = 3(\rho_p - \rho_0)/(2\rho_p + \rho_0)$ and the kinetic energy density $E_k = \rho_0|\mathbf{v}|^2/4$. Hence, this term is related to the particle back and forth relative translation compared to the surrounding fluid. Particles denser than the surrounding fluid, i.e., with $f_2 > 0$ (respectively less dense, $f_2 < 0$), are pushed by this term toward velocity amplitude

maxima (respectively minima). If both the density and compressibility differ and for standing wavefields (wherein the pressure antinodes coincide with velocity nodes), it is convenient to introduce the so-called *acoustic contrast factor* ([32,33])

$$\Phi_{\text{SW}} = \frac{5\rho_p - 2\rho_0}{2\rho_p + \rho_0} - \frac{\kappa_p}{\kappa_0}, \quad (7)$$

whose sign indicates whether particles migrate toward pressure nodes or antinodes. Particles with positive contrast factor $\Phi_{\text{SW}} > 0$ (e.g., most solid particles and typical cells) get trapped at the pressure nodes, while particles with negative contrast factor $\Phi_{\text{SW}} < 0$, (e.g., certain liquids droplets) get trapped at the pressure antinodes.

However, such an analysis with the contrast factor is only valid for standing waves in the Rayleigh regime, since (i) for more complex wavefields, the pressure maxima (minima) do not necessarily coincide with the velocity minima (maxima) (see, e.g., Ref. [31] for a discussion of particle trapping with spherical Bessel beams in the Rayleigh regime), (ii) in cases wherein the gradient forces are small (due to the homogeneity of the kinetic and potential energy density), the scattering force can also play a role, and finally (iii) the radiation force cannot be decomposed into gradient and scattering forces beyond the Rayleigh regime. Hence, for complex wavefields (such as the one-sided focused beam considered here) in the Rayleigh regime, the contributions from the potential and kinetic energies should be considered separately and added. This is why it is interesting to represent both the potential and kinetic energies (proportional to the pressure magnitude square and velocity magnitude square), as is done in Fig. 2. This figure shows that (i) for this type of one-sided focused beam, the focal point corresponds to both pressure and velocity amplitude maxima; (ii) the focusing magnitude and, hence, gradients of the potential energy are stronger than those of the kinetic energy, suggesting that, for equivalent monopolar and dipolar contrast factors, the monopolar term will play a larger role than the dipolar term.

In this paper, we consider many different types of particles and droplets suspended in water, whose properties are summarized in Table I, insonified by the one-sided focused beam represented in Fig. 2. Figure 3 summarizes the expected role played by the monopolar (potential energy) and dipolar (kinetic energy) terms on the particle.

IV. THREE-DIMENSIONAL TRAPPING WITH FOCUSED-BEAM ACOUSTICAL TWEEZERS

In this section, we study two groups of typical particles, which are commonly used in trapping experiments: one group (Pyrex, PS, and PE) consists of materials less

TABLE I. Acoustic properties for particles and fluid medium (water). Density $\rho_{0,p}$, longitudinal speed of sound c_l , shear speed of sound c_t , and compressibility $\kappa = 1/K$ with modulus $K_e = \rho_p(c_l^2 - 4/3c_t^2)$ for an elastic material and $K_f = \rho_p c_l^2$ for a fluid material. Compared with water, the Pyrex, polystyrene (PS), polyethylene (PE), and typical human cells are less compressible, while olive oil, benzene, fat, and polydimethylsiloxane (PDMS) are more compressible. The acoustic contrast factor Φ_{SW} for Rayleigh particles in standing waves is also given for convenience.

Material	$\rho_{0,p}$ (kg/m ³)	c_l (m/s)	c_t (m/s)	κ (1/TPa)	f_1	f_2	$\Phi_{SW} = f_1 + f_2$
Water	1000	1500	...	444			
Pyrex	2230	5640	3280	25	0.942	0.676	1.618
PS	1050	2350	1100	243	0.452	0.048	0.500
PE	1000	2400	1000	225	0.492	0	0.492
Cell	[1000–1210]	[330–440]
Cell (avg)	1105	1535	...	385	0.136	0.098	0.234
PDMS	1030	1030	110	929	-1.091	0.029	-1.062
Olive oil	900	1440	...	535	-0.206	-0.107	-0.313
Benzene	870	1295	...	685	-0.542	-0.142	-0.684
Lipid (fat)	950	1450	...	500	-0.126	-0.052	-0.178

compressible ($f_1 > 0$) and denser ($f_2 > 0$) than the surrounding medium, and the other (olive oil, benzene, and PDMS) uses materials more compressible ($f_1 < 0$) and generally lighter ($f_2 < 0$), except for PDMS, whose density is slightly higher than that of water. Throughout the present work, simulations are run on a computer with two Intel® Xeon® silver CPU processors running at 2.20

GHz using 384 GB of RAM, with the “Windows Pro for Workstations” operating system. The detailed acoustic parameters used for the simulations are listed in Table I.

A. Materials less compressible and denser than the surrounding medium

The most common elastic particles used experimentally, namely Pyrex, PS, and PE belong to this category, as well as most typical human cells [34]. The case of biological particles will be treated separately in Sec. IV C.

1. Radiation forces in the Rayleigh regime

In this section we consider microparticles of $1 \mu\text{m}$ in radius made of three different kinds of material (Pyrex, PS, and PE) and insonified by the acoustic field introduced in Sec. II, with a wavelength over particle size ratio $a/\lambda \approx 0.03 \ll 1$. The axial radiation force F_z and lateral radiation force F_x (represented in the first and last columns of Fig. 4, respectively) are calculated with three different methods: (i) with Gor’kov’s original expression of the gradient force, (ii) with the generalized Gor’kov theory [23], taking into account the scattering contribution [Eq. (6)], and (iii) with the angular spectrum method (ASM) complete expression of the force. As expected, the three calculations give similar results since (i) the calculations are performed in the Rayleigh regime $ka \ll 1$ and (ii) the field is not homogeneous and, hence, the contribution of the gradient force dominates over that of the scattering force. The Gor’kov potential U is represented in columns two and three of Fig. 4. Stable positions correspond to the minima of the Gor’kov potential, while unstable ones correspond to the maxima of the Gor’kov potential.

All these figures show that these types of particles are expelled both laterally and axially from the center of the focused beam. Indeed, the center of the focused beam is both a pressure and velocity magnitude maximum. Since

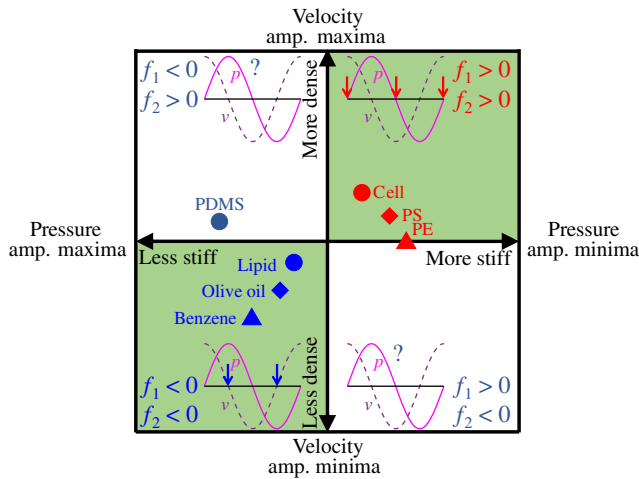


FIG. 3. Quadrant chart explaining in which direction (toward pressure and velocity field maxima or minima) are pushed different types of particles and cells by the monopole and dipole forces depending on the sign of the monopolar and dipolar contrast factors f_1 and f_2 . The referenced medium is water with the acoustic parameters given in Table I. For a 1D standing wave, pressure maxima (antinodes) correspond to velocity minima (nodes). Hence, the movement of the particles in the green quadrants is obvious since both the kinetic and potential forces push in the same directions. In the other quadrants, it is necessary to calculate the contrast factor Φ_{SW} to determine whether particles migrate to the nodes or antinodes. However, the motion is less obvious for focused beams, wherein pressure maxima do not correspond to velocity minima and vice versa.

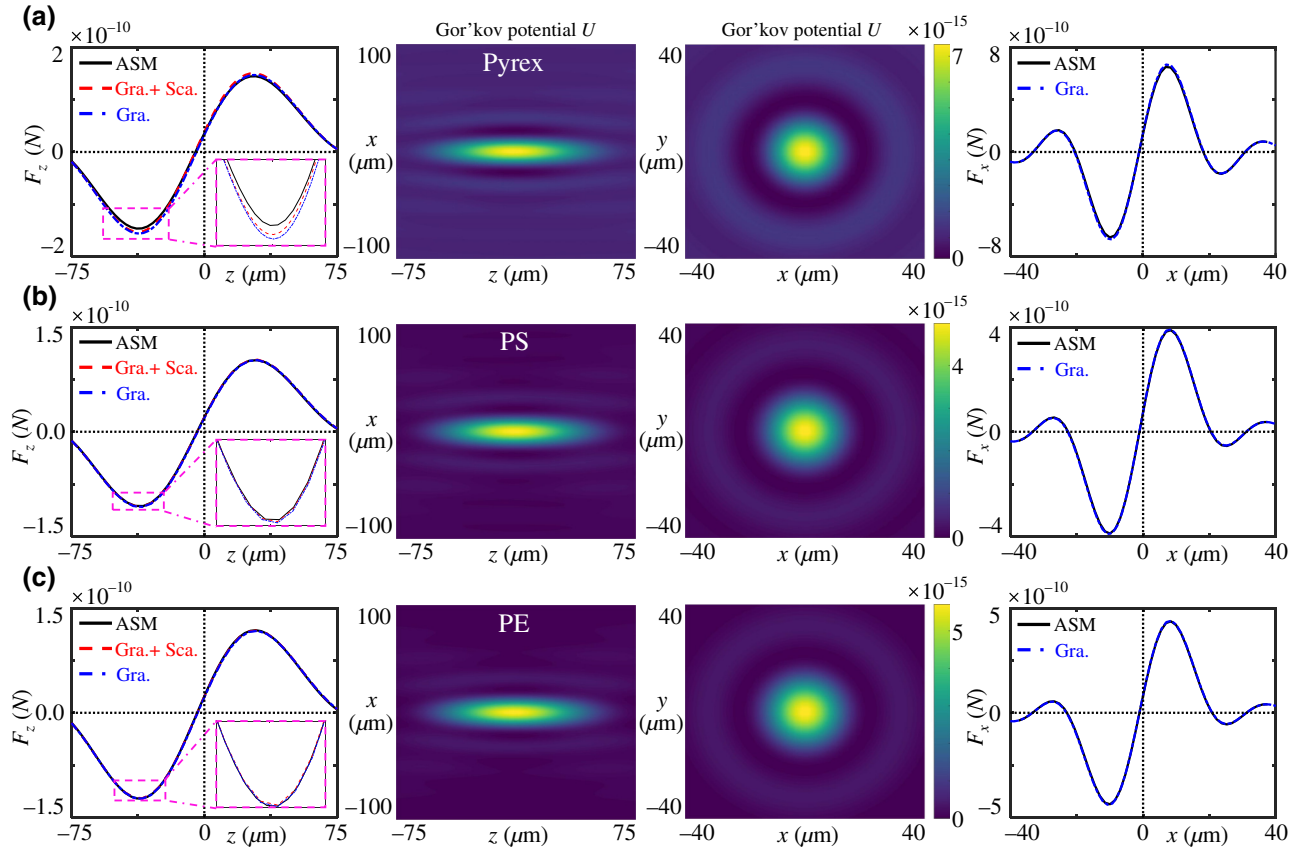


FIG. 4. Axial radiation forces F_z (first column), the Gor'kov potential U (second and third columns; in Nm units), and the lateral radiation force F_x versus spatial positions for (a) Pyrex, (b) PS, and (c) PE particles with radii $a = 1 \mu\text{m}$. The Gor'kov potential U exhibits a maximum in the beam center, indicating that the gradient force $\mathbf{F}_{\text{grad}} = -\nabla U$ pushes the particle away from the focal point. The axial and lateral radiation forces versus their positions are given in the first and fourth columns, respectively. Around the focal point ($x = y = z = 0$) the force is negative (for $z < 0$ and $x < 0$) and then positive (for $z > 0$ and $x > 0$), indicating that this point is repulsive for the particle.

$f_1 > 0$ and $f_2 > 0$, the monopolar (potential energy) and the dipolar (kinetic energy) contributions of the gradient force will respectively push the particle *away* from the beam center and *toward* the beam center. But, since (i) the compressibility contrast is larger than the density contrast for these particles, leading to $f_1 > f_2$, and (ii) the gradients of the potential energy are stronger than the gradient of the kinetic energy (as discussed previously), the monopolar force is dominant and pushes the particles away from the beam center.

2. Resonance scattering theory

Spherical particles constitute some cavities for the wave. Hence, the particles exhibit some resonances when the wavelength of the particle approaches the size of the particle, leading to directional scattering patterns. These resonances play a fundamental role on the radiation force beyond the Rayleigh regime. Hence, it is vital to determine the resonance frequencies of the particle depending on their composition to analyze the results. The resonance

scattering theory developed by Flax *et al.* [35] has been widely used in the literature to isolate the scattering resonances and can predict the correct magnitude of the scattering coefficients. However, it cannot predict the useful phase information. This theory was further improved by Rhee and Park [36], who derived expressions for both the magnitude and phase with the resonance scattering coefficients

$$s_n^{\text{Res}} = \frac{A_n - A_n^b}{1 + 2A_n^b}, \quad (8)$$

where $A_n = (s_n - 1)/2$ and A_n^b are the total and background partial wave coefficients, respectively. For elastic materials, a background scattering from a rigid particle with the same size can be used with the scattering coefficients given in Appendix A 1 to only keep the contribution of the particle resonance. The scattering coefficients for the total (elastic resonance and rigid background) scattering are given in Appendix A 4. This method works quite well for dense metal materials, for example, tungsten carbide

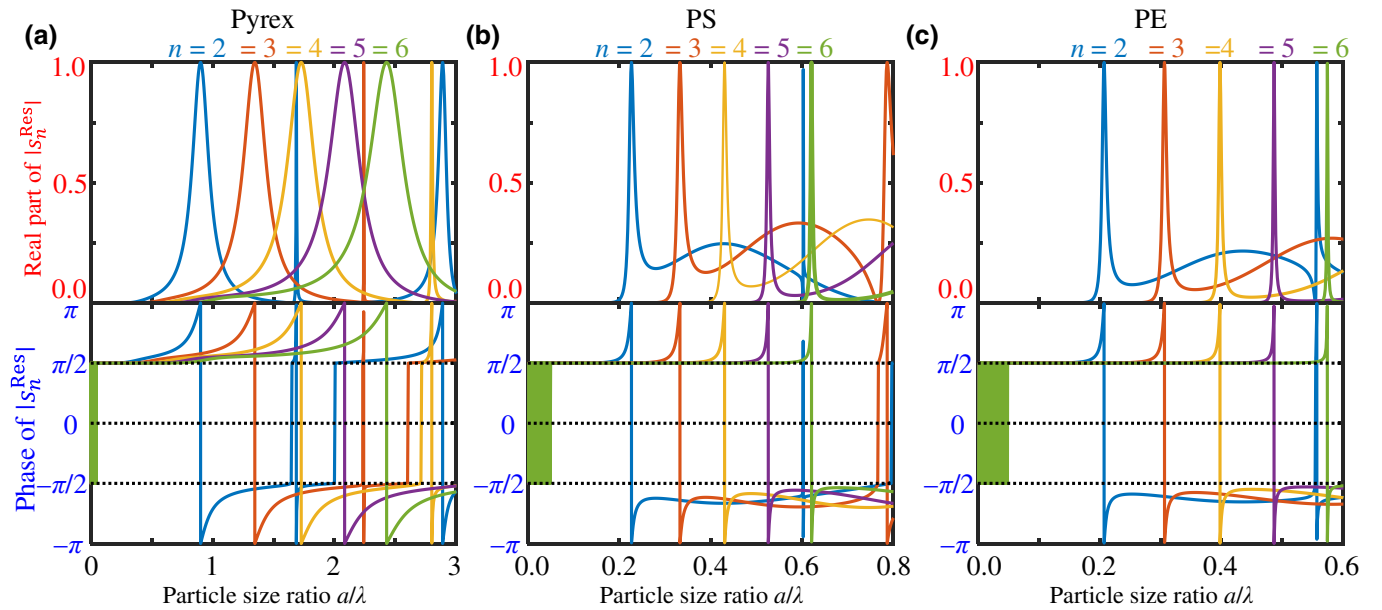


FIG. 5. First resonances of (a) Pyrex, (b) PS, and (c) PE particles. The first row gives the quantity of the real part of the resonance scattering coefficients S_{Res} , while the second row gives the phase information for particle size ratios a/λ from 0 to 3 for Pyrex, from 0 to 0.8 for PS, and from 0 to 0.6 for PE. It is clearly observed that there is a π shift (see the row below) through the resonance peaks (see the upper row). Because the real part is close to 0, the phase has fluctuations π (the imaginary part is positive) and $-\pi$ (negative). The explicit size ratios for different resonances are given in Table II.

with very sharp resonance peaks [37]. The improved method of Rhee and Park is applied for the three materials in the present work. The real part and phase of the resonance scattering coefficients s_n^{Res} with different orders $n \in [2, 6]$ as a function of the particle radius over wavelength ratio a/λ are represented in Fig. 5 for (a) Pyrex, (b) PS, and (c) PE. The sharp peaks in the real part of s_n^{Res} with the corresponding π shift in the phase information provide reliable resonances of orders $n = 2, 3, 4, 5,$ and 6 . The exact values of the radius over wavelength ratio for each resonance are collected in Table II.

3. Three-dimensional radiation forces beyond the Rayleigh regime and 2D trapping

As shown in Sec. IV A 1 for the considered particles, there is no trapping in either the axial or lateral directions in the Rayleigh regime. Here, we study the trapping possibility for these particles beyond the Rayleigh regime

TABLE II. Particle size ratios (a/λ) at resonance frequencies of different orders for Pyrex, PS, and PE materials.

Order	n				
	2	3	4	5	6
Pyrex	0.902	1.347	1.727	2.084	2.428
PS	0.227	0.333	0.431	0.526	0.621
PE	0.207	0.306	0.398	0.486	0.574

based on the angular spectrum method. To obtain a 3D trap, restoring forces (pushing the particle toward the beam center) are required in both the axial and lateral directions, which means that the radiation forces should be negative when the particle is slightly displaced along the z or x axis ($z > 0, x > 0$) and positive when the particle is slightly displaced in the other directions ($z < 0, x < 0$). Of course, the magnitude of the restoring force depends on the exact location of the particle. For simplicity and efficiency, we first calculate the axial and lateral radiation forces as a function of the particle size ratios $a/\lambda = [0, 3]$ at the fixed positions $(x_s, z_s) = (0, 30) \mu\text{m}$ and $(x_s, z_s) = (8, 0) \mu\text{m}$, respectively [see Figs. 6(a), 6(b), 6(c)]. These positions correspond to the maximum of the trapping force in the Rayleigh regime and remain in the central bright spot of the focused wave. An axial trap and a lateral trap at the center of the focused beam can be obtained only if the values of the axial and lateral forces at these positions are negative. Note that this is a necessary but not sufficient condition to obtain a trap. Figure 6 shows that, for Pyrex, PS, and PE particles, the axial force (black curve) is always positive at these positions, hence precluding any possibility for axial trapping of these particles with focused waves. However, close to the particle resonances (calculated in the previous section and represented on these graphs by the dashed curves for $n = [2, 6]$), there are some strong variations of the lateral force, which can become negative, hence suggesting that there is some lateral restoring force. To further demonstrate the 2D lateral trapping ability, three

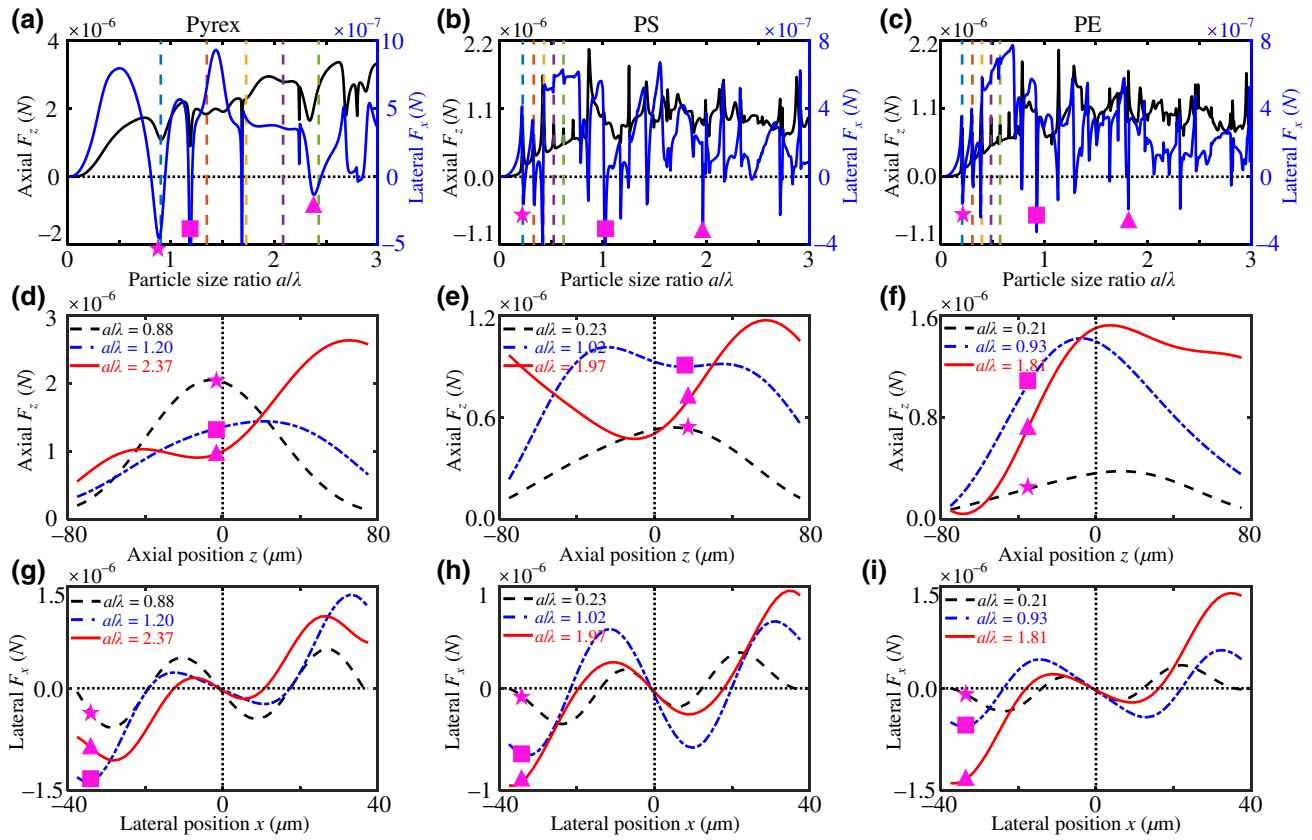


FIG. 6. Three-dimensional acoustical radiation forces based on the angular spectrum method at a fixed axial ($z_s = 30 \mu\text{m}$) and lateral ($x_s = 8 \mu\text{m}$) position for different particle materials: (a) Pyrex, (b) PS, and (c) PE. The left and right vertical axes are respectively the axial (F_z , black solid line) and lateral (F_x , blue solid line) radiation forces, while the horizontal axis shows particle radius over wavelength ratios a/λ from 0 to 3. Three explicit size ratios are chosen (indicated by star, square, and triangle symbols) to show the possibility of two-dimensional trapping, whereas there is no axial trapping beyond the Rayleigh limit for (d),(g) Pyrex with $a/\lambda = 0.88$ (star), 1.20 (square), and 2.37 (triangle); (e),(h) PS with $a/\lambda = 0.23$ (star), 1.02 (square), and 1.97 (triangle); and (f),(i) PE with $a/\lambda = 0.21$ (star), 0.93 (square), and 1.81 (triangle). For the axial radiation force versus z , the lateral position is $x = 0$, while, for the lateral force versus x , the axial position is $z = 0$ here since there is no equilibrium position in this direction. It is possible to have lateral trapping but not axial trapping beyond the Rayleigh regime, while there is no axial or lateral trap in the Rayleigh regime, as shown in Fig. 4.

typical sizes of each particle are selected that have positive axial forces and negative lateral forces [corresponding to the star, rectangle, and triangle marks in Figs. 6(a), 6(b), and 6(c)]. The axial radiation forces versus z on the beam axis are plotted in the second row [Figs. 6(d), 6(e), and 6(f)], and the lateral forces versus x at the focal plane ($z = 0$) are given in the third row [Figs. 6(g), 6(h), and 6(i)]. It is clearly shown that the axial radiation forces are always positive, which will push the particles outside of focus, hence confirming that there is no axial trapping whatever the position of the particle. The lateral force however is positive for $x < 0$ and positive for $x > 0$, confirming the lateral trapping ability at these specific ratios of particle size over wavelength.

4. Conclusion

Our calculations show that Pyrex, PS, and PE particles are always expelled from the focal point in the Rayleigh

regime. Beyond the Rayleigh regime, only lateral trapping of these particles is possible at some specific particle size over wavelength ratios, close to some of the particle resonances. The particle is however always pushed in the axial direction by the radiation force.

B. Materials more compressible and/or less dense than the surrounding medium

The second group of materials (olive oil, benzene, PDMS) considered in this section are more compressible ($f_1 < 0$) and generally lighter ($f_2 < 0$) than the surrounding water, except for PDMS, which is slightly heavier than water.

1. Radiation force in the Rayleigh regime

The same analysis as in Sec. IV A 1 is conducted here for this group of materials. Again, the gradient

force dominates, so Gor'kov's expression is sufficient to estimate the force in the Rayleigh regime. The results represented in Fig. 7 show that all three types of particles are trapped in three dimensions at the focal point of focused beams in the Rayleigh regime. Indeed, PDMS is the perfect solid particle candidate to be trapped by a focused beam in the Rayleigh regime since it is both more compressible and denser than water, leading to $f_1 < 0$ and $f_2 > 0$ and hence to contributions of both the potential and kinetic energies to the gradient force pushing the particle toward the focal point. For olive oil and benzene, f_1 and f_2 are negative. Hence, the gradient of the potential energy pushes the droplet toward the focal point, while the gradient of the kinetic energy pushes the droplet away from the focal point. But, since $|f_1| > |f_2|$ and the gradient of the potential energy is stronger than the gradient of the kinetic energy, the contribution of the monopolar term to the gradient force dominates and hence the droplet is pushed toward the focal point, leading to 3D trapping of the particle. This is clearly seen in the representation of the Gor'kov potential U (columns two and three of Fig. 7), which is minimum at the focal point and from the calculation of the axial and lateral forces (columns one and four of Fig. 7), which are

positive and then negative around the focal point, leading to some restoring force that makes the particle converge toward the beam center.

2. Resonance scattering theory

Again, it is interesting to localize the particle and droplet resonances before studying their ability to get trapped by a focused beam beyond the Rayleigh regime. Since the acoustic impedance of the considered particles and water are close, as shown in Table I, it is not easy to isolate the resonance contribution by subtracting the background from the total scattering field. For a fluid bubble, the scattering from a soft sphere could be taken as the background (see Appendix A 2). However, the soft background is not suitable for the liquid spheres whose density and velocity are close to those of the surrounding water. A more complicated intermediate (hybrid) background may be used [37,38], but this is still an open question. In this work, an alternative method is applied to clarify the resonance sizes for fluid spheres by finding the real roots of $\text{Re}(D_n) = 0$ for different n th partial waves [39], with D_n a parameter

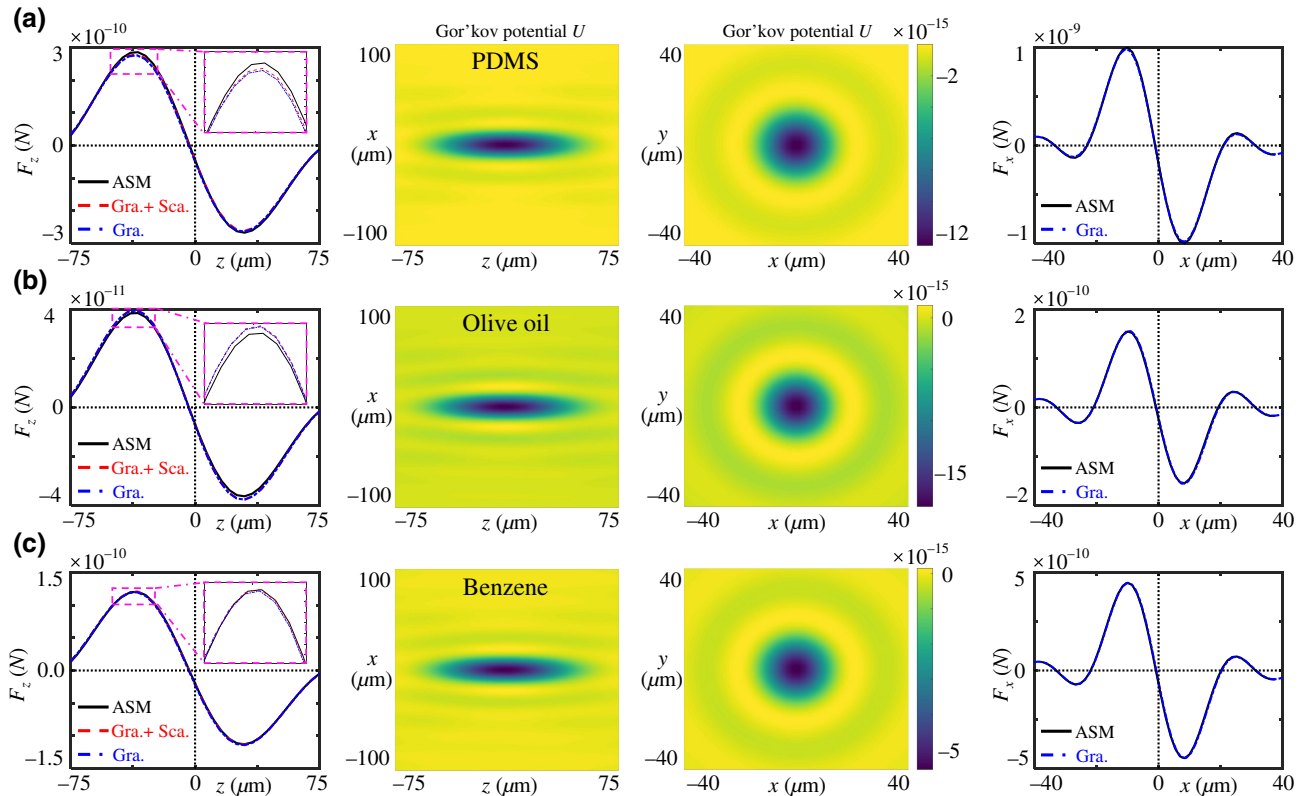


FIG. 7. Axial radiation forces F_z (first column), the Gor'kov potential U (second and third columns; in Nm units), and the lateral radiation force F_x versus spatial positions for (a) PDMS, (b) olive oil, and (c) benzene with particle radius $a = 1 \mu\text{m}$. The Gor'kov potential U exhibits a minimum in the beam center, indicating that the gradient force $\mathbf{F}_{\text{grad}} = -\nabla U$ pushes the particle toward the focal point. The axial and lateral radiation forces versus their positions are given in the first and fourth columns, respectively. The results clearly show a 3D trap at the center of the focused beam for the considered materials.

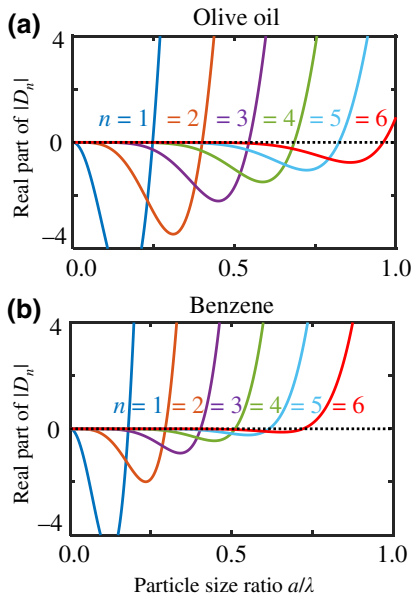


FIG. 8. The resonance frequencies are clarified by finding the zero value of the real part of $|D_n|$ with different order n for fluid particles of (a) olive oil and (b) benzene. The explicit expression of $|D_n|$ for a fluid sphere is given in Appendix A3. The size ratios of different resonances are given in Table III.

introduced for convenience with the relation to the scattering coefficients $s_n = -D_n^*/D_n$ given in Appendix A3. The first several roots are clarified in Fig. 8 for fluid spheres of (a) olive oil and (b) benzene. The explicit resonance size ratios are listed in Table III. Note that the resonance sizes of PDMS spheres are not easy to determine and not discussed here.

3. Three-dimensional radiation forces beyond the Rayleigh regime and 3D trapping

The angular spectrum method is applied to compute the 3D radiation forces for the more compressible particles beyond the Rayleigh regime. The axial and lateral forces versus the particle size ratios a/λ are given in Figs. 9(a)–9(c). Similarly to Fig. 6, the radiation force is first calculated at the axial fixed position $z_s = 30 \mu\text{m}$ on the beam axis and the lateral fixed position is $x_s = 8 \mu\text{m}$ in the focal plane. This time the results show that both axial and lateral negative radiation forces can be observed for some specific size over wavelength ratios, suggesting the

TABLE III. Particle sizes (a/λ) at resonance frequencies for olive oil and benzene.

Order	n					
	1	2	3	4	5	6
Olive oil	0.247	0.400	0.545	0.685	0.824	0.961
Benzene	0.180	0.295	0.404	0.510	0.616	0.721

possibility for 3D trapping. To confirm this, three typical size ratios with negative axial and lateral radiation forces are selected for the three materials and the evolution of the force along the x and z axes is studied. The axial radiation forces versus position z on the beam axis are given in the second row of Fig. 9 for (d) PDMS, (e) olive oil, and (f) benzene, which show the ability of axial trapping. To further study the possibility of 3D trapping, the lateral force versus spatial position x at the axial equilibrium position obtained in (d), (e), and (f) are plotted in the third row. The results confirm 3D trapping capabilities of (i) PDMS spheres with the three selected ratios $a/\lambda = 0.46, 0.83,$ and 1.35 , (ii) olive oil spheres with $a/\lambda = 0.43$, and (iii) benzene spheres with $a/\lambda = 0.39$ and 1.06 . Note nevertheless that, for PDMS, the axial trap is asymmetric and much weaker than the lateral force and that this trend is further accentuated when inelastic scattering (absorption by the particle) is considered (see Appendix B). This is because PDMS strongly absorbs the wave, leading to scattering forces that push the particle in the wave propagation direction. So far, only levitation of these particle in the regime $a/\lambda \in [0.26, 0.52]$ has been reported [13] and 3D trapping of PDMS particles requires further experimental confirmation.

4. Conclusion

The results of this subsection suggest the existence of a 3D radiation trap for PDMS particles and olive oil and benzene droplets at the center of one-sided focused beams both in the Rayleigh regime and beyond the Rayleigh regime at specific frequencies.

C. Biological particles

The manipulation of biological microorganisms such as cells is of primary interest for applications, e.g., to assemble cells for tissue engineering, probe their adherence, or measure their rheological properties. Here we review the abilities of focused beams to trap two types of biological particles, namely typical human cells and lipid cells.

1. Typical human cells

The density and compressibility of typical human cells are taken from Ref. [34] and given in Table I. Typical cells are slightly less compressible and denser than water. Five sets of acoustic parameters corresponding to the extreme and average values of Ref. [34] are considered and the respective axial and lateral radiation forces versus size ratio a/λ are given in Figs. 10(a) and 10(b). Note that these specific values do not correspond to specific types of cells but are used to give tendencies depending on the variation of the compressibility and density. As in the previous sections, the force is first calculated at a fixed axial position $z_s = 30 \mu\text{m}$ and fixed lateral position $x_s = 8 \mu\text{m}$. As observed, the negative axial radiation force only occurs

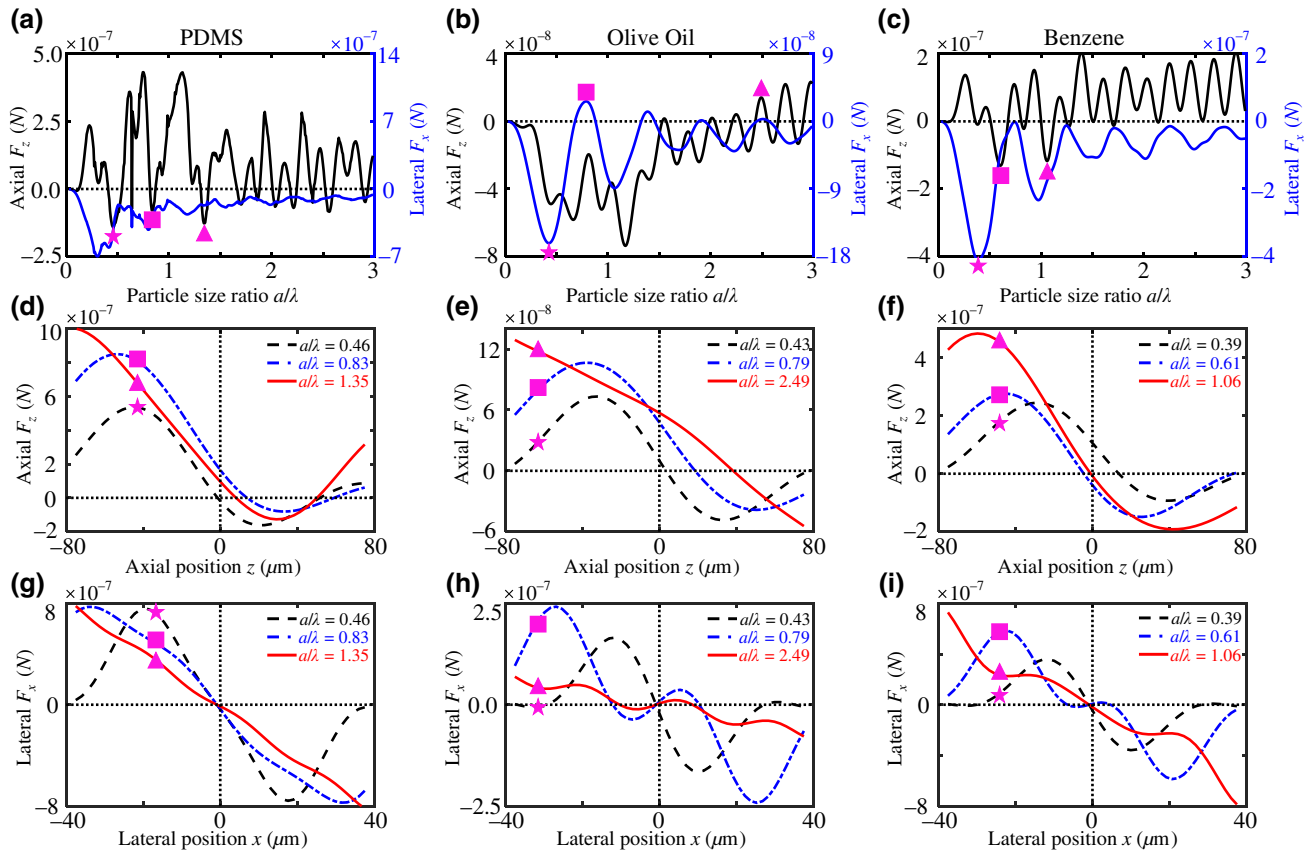


FIG. 9. Three-dimensional acoustical radiation forces based on the angular spectrum method at a fixed axial ($z_s = 30 \mu\text{m}$) and lateral ($x_s = 8 \mu\text{m}$) position for different particle materials: (a) PDMS, (b) olive oil, and (c) benzene. The left and right vertical axes are respectively the axial (F_z , black solid line) and lateral (F_x , blue solid line) radiation forces, while the horizontal axis shows particle radius over wavelength ratios a/λ from 0 to 3. Three explicit size ratios are chosen to show the possibility of three-dimensional trapping beyond the Rayleigh limit for (d),(g) PDMS with $a/\lambda = 0.46$ (star), 0.83 (square), and 1.35 (triangle); (e),(h) olive oil with $a/\lambda = 0.43$ (star), 0.79 (square), and 2.49 (triangle); and (f),(i) benzene with $a/\lambda = 0.39$ (star), 0.61 (square), and 1.06 (triangle). For the axial radiation force versus z , the lateral position is $x = 0$, while the lateral radiation force versus x in the third row is plotted at the axial equilibrium positions obtained in the second row. Three-dimensional trapping is possible for several particle sizes beyond the Rayleigh regime.

for $[\rho, \kappa] = [1210, 440]$, while the negative lateral force is possible for $[\rho, \kappa] = [1000, 440]$, $[1105, 385]$, $[1210, 330]$, and $[1210, 440]$ at certain size over wavelength ratios. This first calculation suggests the possibility of 2D or 3D trapping for human cells with some acoustic parameters in a spherical focused beam. The examples of 2D trapping are given in Figs. 10(c) and 10(d), which clearly show the lateral trapping without axial trapping for the cases $[\rho, \kappa] = [1105, 385]$ with $a/\lambda = 0.81$ and $[\rho, \kappa] = [1210, 330]$ with $a/\lambda = 0.84$. Three-dimensional trapping only occurs for the largest density and compressibility $[\rho, \kappa] = [1210, 440]$ compared with water, as shown in Figs. 10(e) and 10(f). The axial force and lateral force at axial equilibrium position versus spatial positions are calculated for a size ratio $a/\lambda = 0.58$. However, these extreme values might not correspond to existing cells. Typical human cells could however be trapped by using single beam tweezers based on a vortex beam [21].

2. Lipid (fat) cells

The first experiments of single beam trapping with acoustical tweezers based on focused beams were conducted by Lee *et al.* [3] for the oleic acid lipid droplets, and in this work, only lateral 2D trapping was reported. The typical density of lipid cells is $[910\text{--}1010] \text{ kg/m}^3$ [40]. Here, we take the acoustic parameters (density and sound speed) of a lipid droplet from Ref. [5], as listed in Table I. At the fixed axial position $z_s = 30 \mu\text{m}$ and the lateral position $x_s = 8 \mu\text{m}$, the 3D radiation forces versus the size ratios in the designed focused beam are first studied as given in Fig. 11(a), which suggest the possibility for 3D trapping in the range $a/\lambda = 0$ to 2. This is further confirmed by Figs. 11(b) and 11(c), which show the axial and lateral radiation forces versus the spatial position for three selected size ratios: $a/\lambda = 0.5$, 1, and 2. The lateral forces in Fig. 11(c) are calculated at the axial equilibrium position obtained in (b). These figures show both an axial and

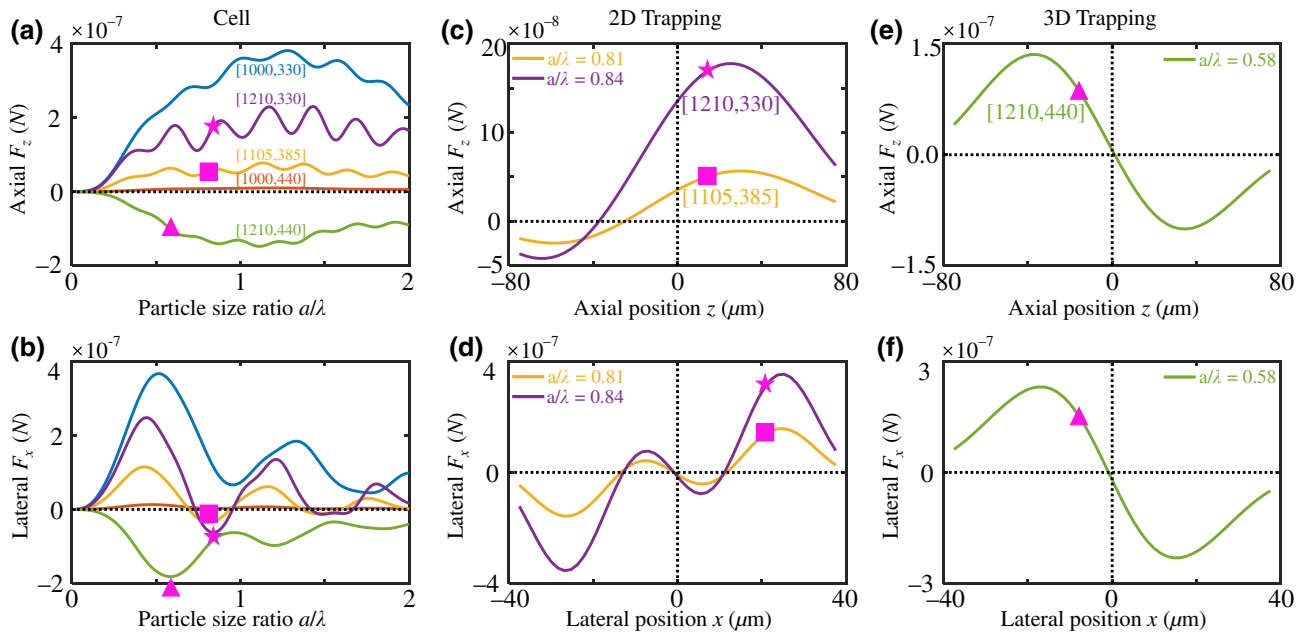


FIG. 10. Three-dimensional acoustical radiation forces based on the angular spectrum method at a fixed axial ($z_s = 30 \mu\text{m}$) and lateral ($x_s = 8 \mu\text{m}$) position for cells with different acoustic parameters of density (kg/m^3) and compressibility ($1/\text{TPa}$) $[\rho, \kappa] = [1000, 330], [1000, 440], [1105, 385], [1210, 330],$ and $[1210, 440]$. (a) Axial force F_z versus particle size ratio a/λ , and (b) lateral force F_x versus a/λ . Panels (c) and (d) give the axial and lateral radiation forces versus position for the fixed particle sizes marked in (b): $a/\lambda = 0.81$ (square) for $[\rho, \kappa] = [1105, 385]$ and $a/\lambda = 0.84$ (star) for $[\rho, \kappa] = [1210, 330]$. Only the lateral 2D trapping is possible. Similar to (c) and (d), (e) and (f) give the axial and lateral three-dimensional radiation forces for a cell with $a/\lambda = 0.58$ (triangle) for $[\rho, \kappa] = [1210, 440]$. For the axial radiation force versus z , the lateral position is $x = 0$. The lateral radiation force versus x is plotted at the axial equilibrium positions in (f), while at $z = 0$ in (d). In this case, a 3D trapping occurs.

lateral restoring force. We further investigate the trapping ability for the size over wavelength ratios used in Ref. [5], i.e., $a/\lambda = 4, 5,$ and 6 . In the angular spectrum method, the truncation number corresponding to the integer $n = N_{\text{max}}$ at which the sums appearing in Eqs. (5) are truncated depends on the orders of the poles that are excited by the incident field. Generally, the truncation number increases with the particle over wavelength ratio, but it also depends on the symmetries of the incident field and particle. Here, to compute the force applied on the particle, the particle is out centered, leading to the absence of symmetry, and, since the size over wavelength ratio is large, the truncation number and hence the computational cost is large. As a consequence, it is hardly possible to calculate the 3D radiation forces versus size ratio as in Fig. 11(a) with our simulation hardware platform within a reasonable computation time. This is why we compute the radiation force only for these specific values and ran some convergence tests as a function of the truncation number [Fig. 11(d)] for the worst case $a/\lambda = 6$. In this case, the truncation number [41] $N_{\text{max}} = 2 + \text{Int}(8 + ka + 4.05\sqrt[3]{ka}) = 62$ for Eqs. (5) is larger than 42, which is the number starting to be convergent in Fig. 11(d), with k the wave number and “Int” denoting the integer part of the indicated argument. For the three calculated ratios $a/\lambda = 4, 5,$ and 6 , the

axial radiation force versus z and the lateral forces versus x at the axial equilibrium position are given in Figs. 11(e) and 11(f), respectively. These figures suggest that 3D trapping of lipid cells at these particle size over wavelength ratios is possible.

3. Conclusion

Our results suggest the possibility (i) of trapping typical human cells in two dimensions, while 3D trapping might be possible only for specific cells with large density and compressibility, and (ii) of trapping lipid cells in three dimensions in Mie and geometric optics regimes at specific frequencies.

V. CONCLUSIONS

Compared to their focused vortex counterpart, single beam acoustical tweezers based on focused beams have several advantages, such as easier synthesis, higher expected selectivity and forces due to stronger gradients, no repulsive ring surrounding the trapped particle, which complexifies particle assembly [31,42], and no rotation of the particle due to angular momentum transfer [28]. But, so far, 3D trapping with focused beams has never been demonstrated. Our numerical analysis shows that single

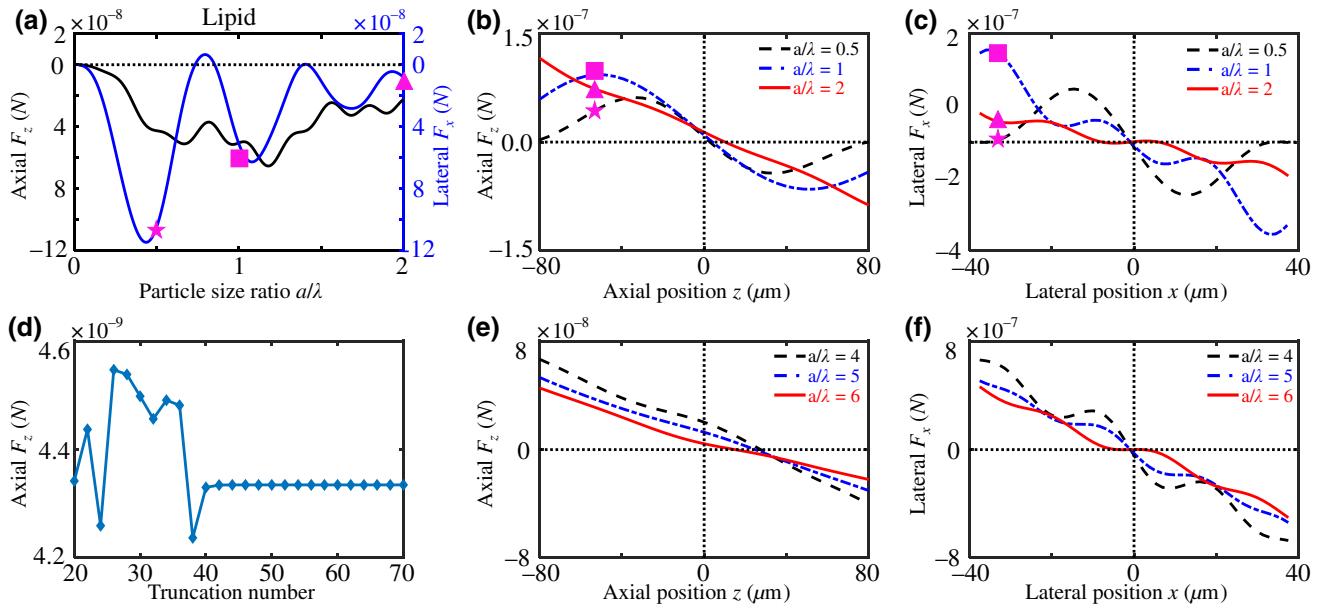


FIG. 11. (a) Three-dimensional acoustical radiation forces based on the angular spectrum method at a fixed axial ($z_s = 30 \mu\text{m}$) and lateral ($x_s = 8 \mu\text{m}$) position for lipid (fat cell) with density $\rho = 950 \text{ (kg/m}^3\text{)}$ and sound speed $c = 1450 \text{ m/s}$. The left and right vertical axes are respectively the axial (F_z , black solid line) and lateral (F_x , blue solid line) radiation forces, while the horizontal axis shows particle radius over wavelength ratios a/λ from 0 to 2. Panels (b) and (c) give the axial and lateral radiation forces versus position for the fixed particle sizes marked in (a) with $a/\lambda = 0.5$ (star), $a/\lambda = 1$ (square), and $a/\lambda = 2$ (triangle). Panel (d) shows a convergence test for high-frequency lipid cell with $a/\lambda = 6$. Panels (e) and (f) give the axial and lateral radiation forces versus position for a fixed particle size with $a/\lambda = 4$, $a/\lambda = 5$, and $a/\lambda = 6$. For the axial radiation force versus z , the lateral position is $x = 0$, while for the lateral force versus x , the axial positions are at the equilibrium positions extracted in (b) and (e). The 3D trapping of lipid cells is possible in the designed focused beam at certain size ratios.

beam acoustical tweezers based on focused beams may have the potential (i) to trap elastic particles and droplets more compressible than the surrounding medium in three dimensions in and beyond the Rayleigh regime; (ii) to trap less compressible particles in the lateral 2D direction for some size ratios near resonances beyond the Rayleigh regime; (iii) to trap lipid cells in three dimensions and typical human cells in two dimensions. This work provides a basis toward the experimental investigation of 3D trapping abilities of droplets, particles, and microorganisms with single beam tweezers based on focused beams. The next step would include experimental confirmation and also calculation and measurement of the streaming produced by the focused beam depending on the actuation frequency and comparison of the streaming-induced drag force to the trapping force.

ACKNOWLEDGMENTS

We acknowledge the support of the ERC Generator, Prematuration, and Talent project programs funded by ISITE Université Lille Nord-Europe. We also thank Prof. Philip L. Marston at Washington State University for helpful discussions on seeking the resonance frequencies of the fluid sphere.

APPENDIX A: SCATTERING COEFFICIENTS OF A SPHERE WITH DIFFERENT MATERIALS

The scattering coefficients of spheres are well known in the literature and were reviewed in the Appendix of Gong's thesis [43]; we recall them hereafter for convenience. Below, k corresponds to the wave number in the fluid medium, a to the radius of the sphere, ρ to the density, and c to the speed of sound at rest, respectively.

1. Rigid sphere

As a background scattering to isolate the resonance contribution of an elastic sphere from the total scattering field, the scattering coefficients of a rigid sphere are

$$s_n = -h_n^{(2)'}(ka)/h_n^{(1)'}(ka), \quad (\text{A1})$$

where the indexes (1) and (2) indicate Hankel functions of the first and second kinds, and the prime represents the derivative with respect to the indicated argument to the dimensionless frequency (ka).

2. Soft sphere

The scattering from a soft sphere can be considered as the background contribution of a bubble in liquid with the

impedance smaller than that of the surrounding medium. The scattering coefficients of a soft sphere are

$$s_n = -h_n^{(2)}(ka)/h_n^{(1)}(ka). \quad (\text{A2})$$

3. Fluid (liquid and air) sphere

In an ideal fluid sphere, only the longitudinal wave exists (no transverse wave). A parameter D_n is introduced for convenience with the relation to the scattering coefficients given by $s_n = -D_n^*/D_n$ [44], where the asterisk indicates the complex conjugate and

$$D_n = \rho_f k a j_n(ka/\gamma_c) h_n^{(1)'}(ka) - \rho (ka/\gamma_c) j_n'(ka/\gamma_c) h_n^{(1)}(ka) \quad (\text{A3})$$

with ρ_f the density of the fluid sphere, $\gamma_c = c_f/c$ the ratio of sound speed in the spherical fluid droplet (c_f) over that in the surrounding fluid c , and j_n the Bessel function of the first kind.

4. Elastic sphere

For an elastic sphere, there are both longitudinal and transverse components of elastic waves with sound speeds c_l and c_t , and wave numbers $k_l = (c/c_l)k$ and $k_t = (c/c_t)k$, respectively. The density of the elastic sphere is ρ_e . It is convenient to define the dimensionless frequency in the fluid medium of the longitudinal wave in the elastic sphere $x_l = k_l a$, and of the transverse wave $x_t = k_t a$. A coefficient is introduced as $N = n(n+1)$ for convenience. The scattering coefficients can be obtained as $s_n = -|D_n^*|/|D_n|$ with D_n consisting of 3×3 elements [45]

$$d_{11} = (\rho/\rho_e) x_s^2 h_n^{(1)}(x), \quad (\text{A4a})$$

$$d_{12} = (2N - x_s^2) j_n(x_p) - 4x_p j_n'(x_p), \quad (\text{A4b})$$

$$d_{13} = 2N [x_s j_n'(x_s) - j_n(x_s)], \quad (\text{A4c})$$

$$d_{21} = -x h_n^{(1)'}(x), \quad (\text{A4d})$$

$$d_{22} = x_p j_n'(x_p), \quad (\text{A4e})$$

$$d_{23} = N j_n(x_s), \quad (\text{A4f})$$

$$d_{31} = 0 \quad (\text{A4g})$$

$$d_{32} = 2[j_n(x_p) - x_p j_n'(x_p)], \quad (\text{A4h})$$

$$d_{33} = 2x_s j_n'(x_s) + (x_s^2 - 2N + 2)j_n(x_s). \quad (\text{A4i})$$

where $|D_n^*|$ and $|D_n|$ denote the determinants of matrices D_n^* and D_n . Note that, for an elastic shell, the explicit elements of D_n are given in Ref. [46].

5. Viscoelastic spherical shell filled with fluid

The scattering coefficients s_n of a viscoelastic shell filled with fluid can be obtained based on the Kelvin-Voigt linear

viscoelastic model [28,47], and calculated from the partial wave coefficients A_n with the relation $A_n = (s_n - 1)/2$, where

$$A_n = -\frac{F_n j_n(x) - x j_n'(x)}{F_n h_n^{(1)}(x) - x h_n^{(1)'}(x)}, \quad (\text{A5})$$

Here, the time harmonics $e^{-i\omega t}$ is applied so that the Hankel function of the first kind should be used. The explicit elements of F_n are given in detail in Appendix A of Ref. [41]. The complex wave number is used when the absorption is considered for the viscoelastic material (i.e., the contribution from the imaginary part). When the imaginary part vanishes, the model turns to an elastic material. In addition, the shell model can degenerate into a solid elastic sphere when the inner fluid is missing.

APPENDIX B: PDMS IN THE VISCOELASTIC MODEL

The Kelvin-Voigt linear viscoelastic model [28,47] is applied to calculate the scattering coefficients as given

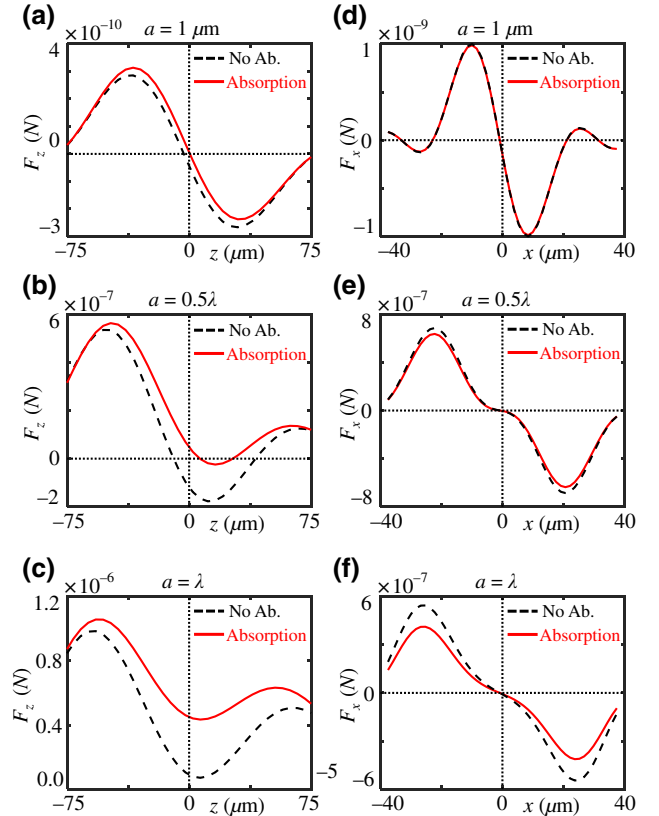


FIG. 12. The three-dimensional radiation forces versus the spatial positions for the PDMS particles with and without absorption in the (a),(b),(c) axial and (d),(e),(f) lateral (at the focal plane $z_s = 0$) directions. Three particle radii are taken into consideration as $a = 1 \mu\text{m}$, 0.5λ , and λ . The wavelength is $\lambda = 37.5 \mu\text{m}$.

in Appendix A5 when the absorption effects are considered inside the PDMS particles. The normalized absorption coefficients of the PDMS are calculated from Ref. [48]. Here, the normalized absorption coefficients of the longitudinal and transverse waves are $\gamma_l = 0.0075$ and $\gamma_t = 0.2673$, respectively. The 3D radiation forces for PDMS particles with and without absorption are studied based on the angular spectrum method with radii $a = 1 \mu\text{m}$, 0.5λ , and λ , as shown in Fig. 12. As shown, the 3D trapping is still possible for small particles when the absorption effect is under consideration, although the axial pushing force increases since the absorption of the linear momentum produces the positive axial radiation force [49]. When the particle size reaches $a = \lambda$, for instance, there is no axial trapping anymore, while lateral trapping is still possible; see Figs. 12(c) and 12(f). This gives us some guidance to use a focused beam to trap compressible elastic particles in three dimensions for experimental demonstration, which has not yet been done to the authors' knowledge. It is noteworthy that the levitation of PDMS particles in the Mie regime ($a/\lambda \approx 1$) by a focused beam using a transducer array has recently been implemented [13]. However, 3D trapping was not demonstrated.

-
- [1] A. Ashkin, J. M. Dziedzic, J. E. Bjorkholm, and S. Chu, Observation of a single-beam gradient force optical trap for dielectric particles, *Opt. Lett.* **11**, 288 (1986).
- [2] J. Wu, Acoustical tweezers, *J. Acoust. Soc. Am.* **89**, 2140 (1991).
- [3] J. Lee, S.-Y. Teh, A. Lee, H. H. Kim, C. Lee, and K. K. Shung, Single beam acoustic trapping, *Appl. Phys. Lett.* **95**, 073701 (2009).
- [4] J. Lee, K. Ha, and K. K. Shung, A theoretical study of the feasibility of acoustical tweezers: Ray acoustics approach, *J. Acoust. Soc. Am.* **117**, 3273 (2005).
- [5] J. Lee and K. K. Shung, Radiation forces exerted on arbitrarily located sphere by acoustic tweezer, *J. Acoust. Soc. Am.* **120**, 1084 (2006).
- [6] F. Zheng, Y. Li, H.-S. Hsu, C. Liu, C. Tat Chiu, C. Lee, H. Ham Kim, and K. K. Shung, Acoustic trapping with a high frequency linear phased array, *Appl. Phys. Lett.* **101**, 214104 (2012).
- [7] X. Chen, K. H. Lam, R. Chen, Z. Chen, P. Yu, Z. Chen, K. K. Shung, and Q. Zhou, An adjustable multi-scale single beam acoustic tweezers based on ultrahigh frequency ultrasonic transducer, *Biotechnol. Bioeng.* **114**, 2637 (2017).
- [8] J. Lee, C. Lee, H. H. Kim, A. Jakob, R. Lemor, S.-Y. Teh, A. Lee, and K. K. Shung, Targeted cell immobilization by ultrasound microbeam, *Biotechnol. Bioeng.* **108**, 1643 (2011).
- [9] H.-C. Liu, Y. Li, R. Chen, H. Jung, and K. K. Shung, Single-beam acoustic trapping of red blood cells and polystyrene microspheres in flowing red blood cell saline and plasma suspensions, *Ultrasound Med. Biol.* **43**, 852 (2017).
- [10] J. Lee, C. Lee, and K. K. Shung, Calibration of sound forces in acoustic traps, *IEEE Trans. Ultrason., Ferroelectr., Freq. Control* **57**, 2305 (2010).
- [11] H. G. Lim, Y. Li, M.-Y. Lin, C. Yoon, C. Lee, H. Jung, R. H. Chow, and K. K. Shung, Calibration of trapping force on cell-size objects from ultrahigh-frequency single-beam acoustic tweezer, *IEEE Trans. Ultrason., Ferroelectr., Freq. Control* **63**, 1988 (2016).
- [12] G. T. Silva, A. Baggio, J. H. Lopes, and F. G. Mitri, Computing the acoustic radiation force exerted on a sphere using the translational addition theorem, *IEEE Trans. Ultrason., Ferroelectr., Freq. Control* **62**, 576 (2015).
- [13] Y. Yang, T. Ma, S. Li, Q. Zhang, J. Huang, Y. Liu, J. Zhuang, Y. Li, X. Du, L. Niu, Y. Xiao, C. Wang, F. Cai, and H. Zheng, Self-navigated 3D acoustic tweezers in complex media based on time reversal, *Research* **2021**, 9781394 (2021).
- [14] R. Lirette, J. Mobley, and L. Zhang, Ultrasonic Extraction and Manipulation of Droplets from a Liquid-Liquid Interface with Near-Field Acoustic Tweezers, *Phys. Rev. Appl.* **12**, 061001 (2019).
- [15] D. Baresch, J.-L. Thomas, and R. Marchiano, Observation of a Single-Beam Gradient Force Acoustical Trap for Elastic Particles: Acoustical Tweezers, *Phys. Rev. Lett.* **116**, 024301 (2016).
- [16] M. Baudoin and J.-L. Thomas, Acoustical tweezers for particle and fluid micromanipulation, *Annu. Rev. Fluid Mech.* **52**, 205 (2020).
- [17] M. Baudoin, J. Gerbedoen, B. M. O. N. Smagin, A. Riaud, and J.-L. Thomas, Folding a focalized acoustical vortex on a flat holographic transducer: Miniaturized selective acoustical tweezers, *Sci. Adv.* **5**, eaav1967 (2019).
- [18] R. Al Sahely, J.-C. Gerbedoen, N. Smagin, R. Chutani, O. Bou Matar, and M. Baudoin, Ultra-high frequency vortex-based tweezers for microparticles manipulation with high spatial selectivity and nanonewton forces, (to be published 2022).
- [19] M. Baudoin, J.-L. Thomas, R. Al Sahely, J.-C. Gerbedoen, Z. Gong, A. Sivery, O. B. Matar, N. Smagin, P. Favreau, and A. Vlandas, Spatially selective manipulation of cells with single-beam acoustical tweezers, *Nat. Commun.* **11**, 4244 (2020).
- [20] A. Riaud, M. Baudoin, O. Bou Matar, and J.-L. Thomas, Selective Manipulation of Microscopic Particles with Precursor Swirling Rayleigh Waves, *Phys. Rev. Appl.* **7**, 024007 (2017).
- [21] Z. Gong and M. Baudoin, Three-Dimensional Trapping and Dynamic Axial Manipulation with Frequency-Tuned Spiraling Acoustical Tweezers: A Theoretical Study, *Phys. Rev. Appl.* **16**, 024034 (2021).
- [22] D. Baresch and V. Garbin, Acoustic trapping of microbubbles in complex environments and controlled payload release, *Proc. Nat. Ac. Sci. USA* **117**, 15490 (2020).
- [23] O. A. Sapozhnikov and M. R. Bailey, Radiation force of an arbitrary acoustic beam on an elastic sphere in a fluid, *J. Acoust. Soc. Am.* **133**, 661 (2013).
- [24] Z. Gong and M. Baudoin, Equivalence between multipole expansion based and angular spectrum based three-dimensional acoustic radiation force and torques formulas, *J. Acoust. Soc. Am.* **149**, 3469 (2021).

- [25] G. Silva, An expression for the radiation force exerted by an acoustic beam with arbitrary wavefront, *J. Acoust. Soc. Am.* **130**, 3541 (2011).
- [26] B. D. J. Thomas and R. Marchiano, Three dimensional acoustic radiation on an arbitrary located elastic sphere, *J. Acoust. Soc. Am.* **133**, 25 (2013).
- [27] G. Silva, T. Lobo, and F. Mitri, Radiation torque produced by an arbitrary acoustic wave, *Europhys. Lett.* **97**, 54003 (2012).
- [28] Z. Gong and M. Baudoin, Acoustic radiation torque on a particle in a fluid: An angular spectrum based compact expression, *J. Acoust. Soc. Am.* **148**, 3131 (2020).
- [29] L. P. Gorkov, On the forces acting on a small particle in an acoustical field in an ideal fluid, *Sov. Phys. Dokl.* **6**, 773 (1962).
- [30] J. Leão-Neto and G. T. Silva, Acoustic radiation force and torque exerted on a small viscoelastic particle in an ideal fluid, *Ultrasonics* **71**, 1 (2016).
- [31] Z. Gong and M. Baudoin, Three-Dimensional Trapping and Assembly of Small Particles with Synchronized Spherical Acoustical Vortices, *Phys. Rev. Appl.* **14**, 064002 (2020).
- [32] A. Lenshof and T. Laurell, Continuous separation of cells and particles in microfluidic systems, *Chem. Soc. Rev.* **39**, 1203 (2010).
- [33] H. Bruus, Acoustofluidics 7: The acoustic radiation force on small particles, *Lab Chip* **12**, 1014 (2012).
- [34] P. Augustsson, J. T. Karlsen, H.-W. Su, H. Bruus, and J. Voldman, Iso-acoustic focusing of cells for size-insensitive acousto-mechanical phenotyping, *Nat. Commun.* **7**, 11556 (2016).
- [35] L. Flax, G. C. Gaunaurd, and H. Überall, in *Physical acoustics*, (Elsevier, New York, 1981), Vol. 15, p. 191.
- [36] H. Rhee and Y. Park, Novel acoustic wave resonance scattering formalism, *J. Acoust. Soc. Am.* **102**, 3401 (1997).
- [37] W. Li, Q. Gui, and Z. Gong, Resonance scattering of an arbitrary Bessel beam by a spherical object, *IEEE Trans. Ultrason. Ferroelectr. Freq. Control* **66**, 1364 (2019).
- [38] G. Gaunaurd and M. Werby, Sound scattering by resonantly excited, fluid-loaded, elastic spherical shells, *J. Acoust. Soc. Am.* **90**, 2536 (1991).
- [39] P. L. Marston, Gtd for backscattering from elastic spheres and cylinders in water and the coupling of surface elastic waves with the acoustic field, *J. Acoust. Soc. Am.* **83**, 25 (1988).
- [40] G. E. Neurohr and A. Amon, Relevance and regulation of cell density, *Trends Cell Biol.* **30**, 213 (2020).
- [41] Z. Gong, P. L. Marston, and W. Li, Reversals of Acoustic Radiation Torque in Bessel Beams Using Theoretical and Numerical Implementations in Three Dimensions, *Phys. Rev. Appl.* **11**, 064022 (2019).
- [42] Z. Gong and M. Baudoin, Particle Assembly with Synchronized Acoustic Tweezers, *Phys. Rev. Appl.* **12**, 024045 (2019).
- [43] Z. Gong, Ph.D. dissertation, Huazhong University of Science and Technology, Wuhan, China, 2018.
- [44] P. L. Marston, Axial radiation force of a Bessel beam on a sphere and direction reversal of the force, *J. Acoust. Soc. Am.* **120**, 3518 (2006).
- [45] G. Gaunaurd and H. Überall, RST analysis of monostatic and bistatic acoustic echoes from an elastic sphere, *J. Acoust. Soc. Am.* **73**, 1 (1983).
- [46] S. G. Kargl and P. L. Marston, Observations and modeling of the backscattering of short tone bursts from a spherical shell: Lamb wave echoes, glory, and axial reverberations, *J. Acoust. Soc. Am.* **85**, 1014 (1989).
- [47] G. Gaunaurd and H. Überall, Theory of resonant scattering from spherical cavities in elastic and viscoelastic media, *J. Acoust. Soc. Am.* **63**, 1699 (1978).
- [48] G. Xu, Z. Ni, X. Chen, J. Tu, X. Guo, H. Bruus, and D. Zhang, Acoustic Characterization of Polydimethylsiloxane for Microscale Acoustofluidics, *Phys. Rev. Appl.* **13**, 054069 (2020).
- [49] L. Zhang and P. L. Marston, Geometrical interpretation of negative radiation forces of acoustical Bessel beams on spheres, *Phys. Rev. E* **84**, 035601 (2011).